Rotordynamic Analysis of Rotor–Stator Rub Using Rough Surface Contact

Philip Varney[1]

Woodruff School of Mechanical Engineering,
Georgia Institute of Technology,
Atlanta, GA 30318
e-mail: pvarney3@gatech.edu

Itzhak Green

Professor
Woodruff School of Mechanical Engineering,
Georgia Institute of Technology,
Atlanta, GA 30318
e-mail: itzhak.green@me.gatech.edu

Undesirable rotor–stator rub is frequently observed in rotordynamic systems, and has been the subject of many investigations. Most of these studies employ a simple piecewise-smooth linear-elastic contact model (LECM), where the rotor switches between noncontacting and contacting operation once the clearance is exceeded (various complications have been incorporated, though the essential model premises endure). Though useful as a first step, the LECM relies on an arcane contact stiffness estimate, and therefore does not emulate the actual contacting surfaces. Consequentially, the LECM fails to elucidate how real surface parameters influence contact severity and surface durability. This work develops a novel model for rotor–stator rub which is commensurate with reality by treating the surfaces as a collection of stochastically distributed asperities. Specifically, the elastoplastic Jackson–Green (JG) rough surface contact model is used to calculate the quasistatic contact force as a function of rotor displacement, where bulk material deformation and surface cumulative damage are ignored. A simple exponential fit of the contact force is proposed to reduce computational burden associated with evaluating the JG rough surface contact model at each simulation time step. The rotor's response using the LECM and JG rough surface contact model is compared via shaft speed bifurcations and orbit analysis. Significant differences are observed between the models, though some similarities exist for responses with few contacts per rotor revolution.
[DOI: 10.1115/1.4032515]

1 Introduction

Increases in turbomachine efficiency are often achieved via higher operating speeds, lighter shafts, and precisely manufactured bearings with reduced fluid film clearances. Unfortunately, these changes increase the probability of machine faults such as shaft fatigue cracking [1–3] and rotor–stator contact (i.e., rub) [4,5]. Though rare, shaft fatigue cracking is extremely dangerous. On the other hand, rotor–stator rub commonly occurs and can result in decreased machine life via increased wear, heightened susceptibility to fatigue, and adverse thermal effects, in addition to decreased effectiveness of associated fluid-film triboelements. Detecting and preventing rotor–stator rub require detailed knowledge of the conditions precipitating and following the onset of contact.

Rotor–stator rub occurs when the rotor's deflection exceeds the allowable clearance between the rotor and stator. Accurately simulating rotor–stator rub requires realistic and physically meaningful contact models. The first analytic rotor–stator rub investigations simulated rotor–stator rub by truncating the rotor's synchronous imbalance response [4,6]. The truncated waveform was approximated using a Fourier series, which validated for the first time an experimentally observed rotor–stator rub phenomenon: higher harmonic shaft speed oscillations. Though enlightening as a first step, the truncation approach only heuristically approximates the rotor's response, and cannot be considered a true rotor–stator rub model.

To remedy the lack of a true rotordynamic contact model, Beatty [6] introduced the LECM. Once the rotor exceeds the prescribed clearance, a normal restoring force is generated at the interface which is proportional to the rotor–stator interference by the postulated linear contact stiffness k_c; the original work assumes a linear force–interference relationship, as do many

subsequent investigations. Though other rotordynamic contact models have been introduced since the LECM, such as Choy and Padovan's rub-energy contact model [7], a majority of authors investigating rotor–stator rub have employed some variation of the LECM [8–20]. Various complications to the LECM have been introduced, such as velocity-dependent friction, static offset between the rotor and stator [21], Hertzian contact forces [22,23], and contact damping [22,24], among numerous others. Still, the most prevalent contact models (LECM and Hertzian) assume that the rotor–stator contact force is generated via bulk material deformation, regardless of the contact severity. The LECM has been used to predict a strong nonlinear behavior in the rotor–stator rub systems, such as quasiperiodic and chaotic responses. Bifurcation studies on various system parameters have been performed (such as rotor shaft speed, eccentricity, clearance, and many others), indicating period-doubling, intermittency, and direct transition as possible routes to chaos [9,16,24,25].

Even though the LECM has enjoyed widespread application, and demonstrated some ability to qualitatively predict the rotor response, the model is dissociated from the true nature of contacting surfaces. Estimating the contact stiffness is an inextricable complication and a principle disadvantage of the LECM. Large contact stiffnesses are often assumed, but realistically estimating the contact stiffness is difficult. Even disregarding the complication of estimating the contact stiffness, resistance to surface penetration is clearly nonlinear [26]. In addition, the LECM assumes that rotor–stator rub occurs only at the point of maximum interference. As will be discussed in greater detail later, Varney and Green [27,28] addressed these deficiencies by considering the rotor and stator as curved conformal bodies with finite surface roughness. Real engineering surfaces are not smooth, but instead are composed of peaks, or asperities, of varying height (i.e., real surfaces are rough). Greenwood and Williamson [29] reduced the contact of rough elastic surfaces to that of a single composite rough surface in contact with a rigid flat, where each asperity is hemispherical and deforms according to Hertzian contact theory. The contact force is then related to the surface separation distance using an assumed stochastic distribution of surface heights. Still,
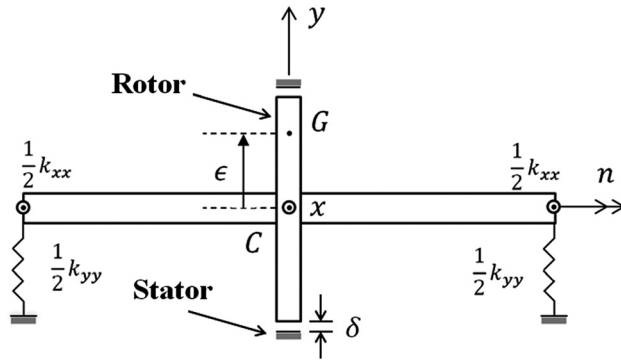
Fig. 1 Jeffcott rotor with finite rotor–stator set-point clearance δ

the Greenwood–Williamson (GW) model considers only elastic deformation, and neglects the possibility of plastic deformation.

In fact, asperity deformation is typically some combination of elastic and plastic effects [30]. A novel rough surface contact model concerning elastoplastic asperity deformation is provided by Chang et al. [31] (i.e., the Chang-Etsion-Bogy (CEB) model. A closed-form solution to the CEB model is provided by Green [32]. Though the CEB model provides useful conceptual understanding of an elastoplastic rough surface contact, the model is not without its shortcomings (namely, the CEB model can predict higher load carrying capacity for a surface deforming elastoplastically than a surface deforming only elastically). Jackson and Green [33] resolved these issues by applying finite element methods to a single hemispherical elastoplastic asperity [30], and extended the results to rough surface contact. Importantly, the JG elastoplastic rough surface contact model accounts for variations in the geometrical hardness of each asperity as a function of deformation. However, the additional accuracy gained by using the JG model comes at an increased computational cost, as additional numeric integrations are required to evaluate the contact force.

As a first step toward improving rotor–stator rub modeling, Varney and Green [27,28] studied the static conformal contact between two curved rough surfaces using the JG elastoplastic rough surface contact model and compared the results to those predicted by the LECM. Their results intuitively indicate that contact between strongly conformal surfaces (i.e., a rotor and stator system with a small set-point clearance) generates a wide circumferential range of non-negligible contact pressure. Furthermore, the force–displacement curve obtained from the JG model is shown to be fundamentally different from that predicted by the

LECM, as the contact force gradually increases as a greater number of asperity contacts accumulate (whereas the LECM suddenly switches on once the rotor deflection exceeds the set-point clearance). The study concludes by providing a simple exponential curve-fit to the quasistatic JG contact force as a function of rotor deflection for a representative set of triboelement surface parameter measurements. As will be seen herein, such an approximation greatly reduces computation time in a rotor–stator rub simulation, as tedious numeric integrations of the asperity contact pressures are avoided at each simulation time step.

Here, for the first time, rough surface contact is applied to model rotor–stator rub dynamics. Rather than assuming a rotor–stator contact stiffness, as is the case with the LECM, measurable rotor and stator surface and material properties are used to obtain the contact force, which is formulated on underlying physical principles rather than simplifying assumptions. Specifically, the JG elastoplastic rough surface contact model is used here according to the methods developed by Varney and Green [28]. Results are provided in the form of rotor orbits, Poincaré sections, and shaft speed bifurcations.

2 Modeling

2.1 Modeling: Rotordynamic System. An elastically supported Jeffcott rotor is shown in Fig. 1, where the support stiffness k is defined in the inertial xyz reference frame. This study considers only cylindrical modes, and consequentially two rotor degrees-of-freedom u_x and u_y are selected, chosen as the deflection of the rotor's geometric center C, referenced from the undeflected position of the rotor O (here, shaft flexibility and conical modes are not considered). The well-known equations of motion for the Jeffcott rotor with constant shaft speed n, including a rotating imbalance and gravity, are

$$m\ddot{u}_x + c\dot{u}_x + ku_x = m\epsilon n^2 \cos(nt) \qquad (1)$$

$$m\ddot{u}_y + c\dot{u}_y + ku_y = m\epsilon n^2 \sin(nt) - mg \qquad (2)$$

The rotor mass is m while the composite viscous damping coefficient resulting from external damping of the disk and support damping is c. The symmetric support has stiffness k, though the symmetry assumption could be easily removed (here, $k_{xx} = k_{yy} = k$). The rotor's center of mass is offset from the geometric center by the eccentricity ϵ. The rotor is constrained within a stationary housing (i.e., the stator) with set-point clearance δ (shown exaggerated in Fig. 2; in reality, the radius of the rotor is significantly greater than the clearance).
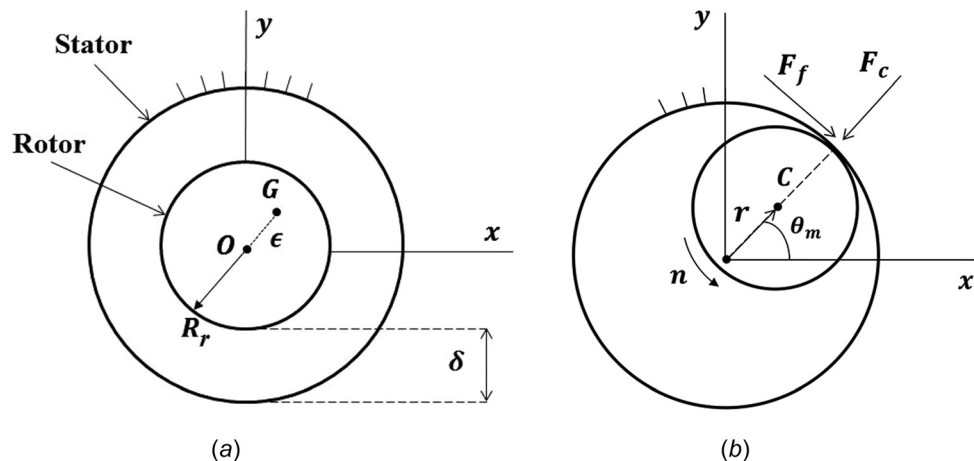

Fig. 2 Lateral contact in the Jeffcott rotor. (*a*) Undeflected rotor–stator system and (*b*) deflected rotor with lateral contact.

As the rotor and stator draw sufficiently close, the asperities on each rough surface interact, generating a contact pressure whose normal and tangential components are $\rho(\theta, z)$ and $\tau(\theta, z)$. Circumferential position is designated by θ, while the rotor's dimension along the axis of rotation is z. Integrating the normal component of the contact pressure over the contact area gives the resultant contact forces in the x and y directions

$$F_{cx} = R_r \int_0^{2\pi} \int_{-B/2}^{B/2} \rho(\theta, z)\cos\theta \, dz \, d\theta \qquad (3)$$

$$F_{cy} = R_r \int_0^{2\pi} \int_{-B/2}^{B/2} \rho(\theta, z)\sin\theta \, dz \, d\theta \qquad (4)$$

where B is the rotor's length into the page and R_r is the rotor radius. Since only lateral deflections are considered, the contact pressure $\rho(\theta)$ is a function of only circumferential position, and the contact force integrals reduce to

$$F_{cx} = R_r B \int_0^{2\pi} \rho(\theta)\cos\theta \, d\theta \qquad (5)$$

$$F_{cy} = R_r B \int_0^{2\pi} \rho(\theta)\sin\theta \, d\theta \qquad (6)$$

Here, a Coulomb model is used to correlate the friction force to the normal contact force, where the dry friction coefficient is μ. Hence, the resultant friction forces in the x and y directions are

$$F_{fx} = \mu F_{cy} \qquad (7)$$

$$F_{fy} = \mu F_{cx} \qquad (8)$$

where the direction of the friction force obeys the convention established in Fig. 2(*b*). It is well-known that certain shaft speeds and parameter ranges can result in the friction force reversing directions, depending on the relative velocity at the contact interface. This switching phenomenon is not observed for the parameter ranges considered herein, as indicated by simulation, and is therefore neglected in the derivations for brevity.

The equations of motion modified to include contact at the rotor–stator interface are

$$m\ddot{u}_x + c\dot{u}_x + ku_x = m\epsilon n^2 \cos(nt) - F_{cx} + F_{fx} \qquad (9)$$

$$m\ddot{u}_y + c\dot{u}_y + ku_y = m\epsilon n^2 \sin(nt) - F_{cy} - F_{fy} - mg \qquad (10)$$

3 Modeling: Calculating the Contact Force

A necessary prerequisite for calculating the contact force is an expression relating the rotor–stator circumferential clearance $h(\theta)$ to circumferential position θ (see Fig. 3). This circumferential clearance expression is obtained here by modifying well-known journal bearing film thickness equations, as prescribed by Varney and Green [28]. Such an approach is permissible when the set-point clearance δ is much smaller than the rotor and stator radii.

Consider a rotor deflected radially by r and oriented from the inertial x axis by θ_m. The clearance between the rotor and stator is then a function of only circumferential position

$$h(\theta) = \delta[1 - (r/\delta)\cos(\theta - \theta_m)] \qquad (11)$$

where θ is defined from the inertial x axis. As the circumferential clearance approaches the surface roughness dimension, the asperities on each surface begin to interact and deform, generating contact pressure between the surfaces. The JG [33] rough surface contact model has previously been shown to compare favorably against other rough surface contact models when compared to
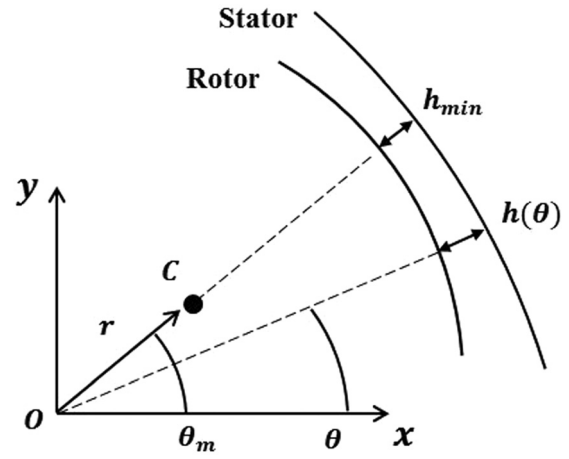

Fig. 3 Clearance between the rotor and stator as a function of circumferential position

experimental results, and will be employed here according to the procedure established by Varney and Green [28]. A summary of the approach is provided in Appendix A. Importantly, bulk deformation of the rotor and stator material is neglected when calculating the contact force. This assumption is reasonable, as the rotor typically rebounds from the stator when only a small percentage of the asperities are in contact (as will be seen herein). Furthermore, cumulative surface damage (i.e., time-varying surface parameters) is not considered herein for simplicity, though such a consideration may be required in future work.

The JG rough surface contact model neglects dynamic effects at each asperity, and consequentially the contact force is strictly quasistatic (as is the LECM). Thus, Varney and Green [28] used regression analysis to obtain a closed-form exponential force–displacement relationship. This closed-form relationship, obtained from a single simulation of rotor displacement versus contact force, can then be implemented in a dynamic simulation of Eqs. (9) and (10) to avoid time-consuming numeric integrations required by the JG model. By first identifying via simulation a suitable range of rotor deflections r_{int} over which rebound occurs, Varney and Green [28] proposed a simple exponential fit

$$\tilde{F}_c = a_1 \exp(\lambda \tilde{r}) - a_0 \qquad (12)$$

where the following normalizations are used for robustness:

$$\tilde{F}_c = F_c / \max(F_c) \qquad (13)$$

$$\tilde{r} = \frac{r - \min(r_{\text{int}})}{\delta \mu_r} \qquad (14)$$

The radial deflection range of interest r_{int} is scaled by the set-point clearance δ and standard deviation of the considered normalized radial deflections μ_r. It is imperative to note that the maximum and minimum values specified in the above equations pertain specifically to the radial contact range of interest. The upper bound of this range is the distance at which asperity interactions become meaningful (i.e., generate a significant contact force). The lower bound of this range is identified via full numeric simulation, as will be discussed in Sec. 4.1. The contact force F_c is normalized by the maximum force obtained in the interval of interest. The specific coefficients a_0, a_1, and λ will be provided where appropriate, in reference to specific presented results (keep in mind that these coefficients are specific to the material properties, surface topography, and considered range of rotor–stator interference).

3.1 Fundamental Differences Between the LECM and JG Contact Models. The LECM and JG rotor–stator rub models are fundamentally different, both qualitatively and quantitatively.
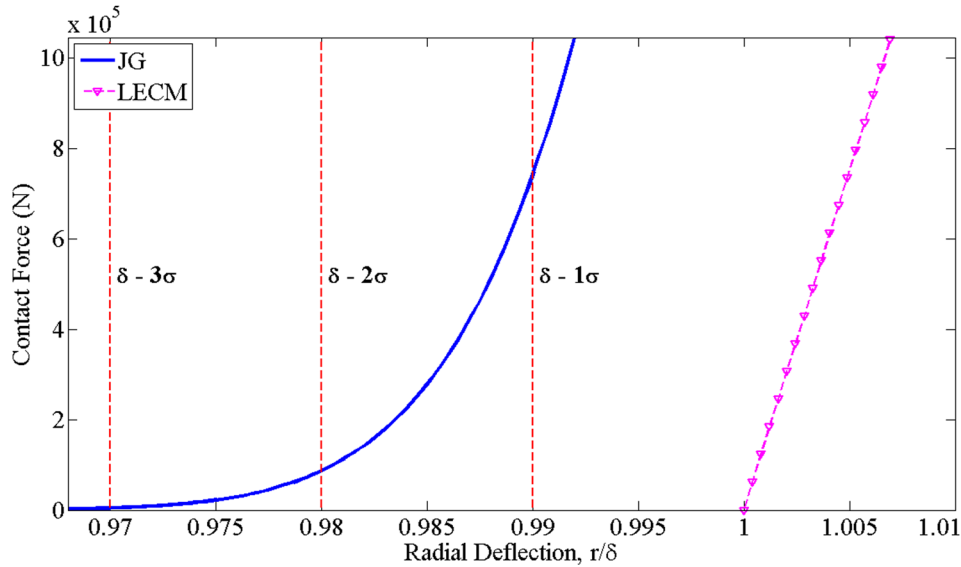
Fig. 4 Comparing the LECM and the JG rough surface contact model [28]

The force–displacement relationship found using both the LECM and JG contact models is shown in Fig. 4 using the representative surface parameters provided by Varney and Green [28] and a linear contact stiffness of $k_c = 1.5 \times 10^8$ N/m in the LECM. From Fig. 4, it is clear that the LECM switches on when the rotor deflection r exceeds the clearance δ. On the other hand, the JG rough surface contact model causes the contact force to gradually increase as more asperities interact on the rotor and stator surfaces. Additionally, the JG rough surface contact model predicts a nonlinear force–displacement relationship, whereas the LECM is linear once contact occurs (however, note that the switching behavior causes nonlinearity in the system even though the LECM force–displacement relationship is by itself linear). Taking into account these differences, the most important distinction between the models is that the JG rough surface contact model does not rely on any a priori choice of parameters, but is instead generated using real and measurable surface parameters.

4 Results

The equations of motion are placed into state-space form and integrated numerically using MATLAB®'s hybrid fourth-/fifth-order variable-step Runge–Kutta solver, ode45. The integration tolerances must be carefully selected due to small rotor–stator interferences; here, the relative and absolute tolerances are set to 10^{-12} and 10^{-15}, respectively. Appropriate tolerances are selected by progressively tightening the tolerance until convergence is obtained. One-tenth of the rotor's static deflection is used as the initial condition in each case, with zero initial velocity; the system is then set into motion via the nonautonomous terms in Eqs. (9) and (10). This work considers only the rotor's steady-state response. Time has been nondimensionalized by the shaft speed, n, such that the nondimensional time is given by $\tau = nt$. The rotor and surface parameters used here are tabulated in Appendix B. The rough surface parameters used herein are calculated from real surface profilometry measurements [32].

4.1 Approximating the JG Contact Force. The first step in expediently simulating the rotor–stator response using the JG rough surface contact model is to obtain a closed-form exponential fit of the quasistatic contact force versus rotor radial deflection, according to the convention established in Eq. (12) (in the author's experience, this curve-fit approach provides computational time savings of at least two orders of magnitude). Therefore, a suitable range of radial deflections over which impact

occurs must be found by full numeric simulation (i.e., fully evaluating the numeric integrations detailed in Appendix A). Such a response is shown in Fig. 5 using the rotor and surface parameters provided in Appendix B. Note that the rotor radial deflection waveform is expressed as rotor–stator closeness, which is defined as the distance between the rotor and stator ($\delta - r$). For clarity, this term is then normalized by the composite surface height standard deviation, σ. Only a small segment of the rotor response is shown here to highlight a single indicative impact (the complete steady-state rotor orbit is shown in Fig. 6(b)).
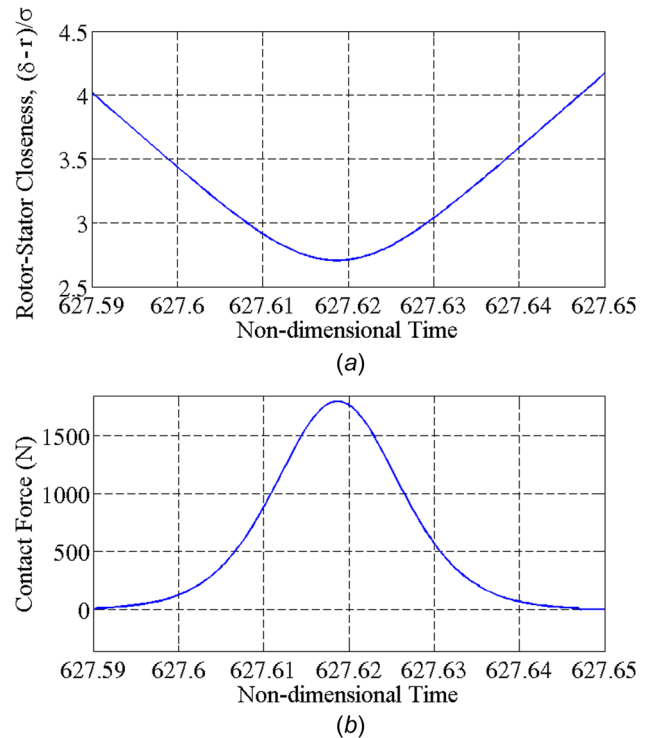

(a)

(b)

Fig. 5 Identifying the radial range over which impact occurs (a) rotor–stator closeness (i.e., separation distance) expressed in multiples of the surface height standard deviation, σ and (b) corresponding contact force
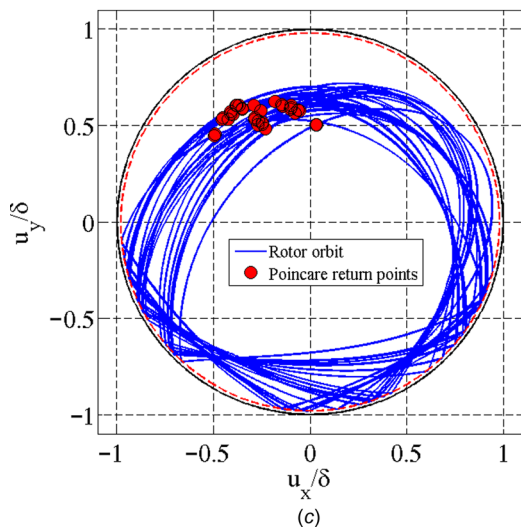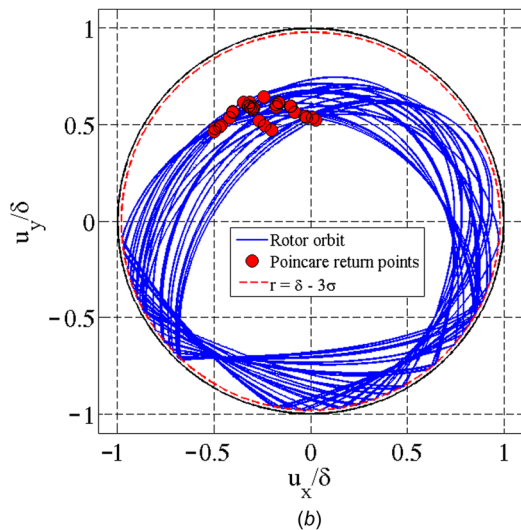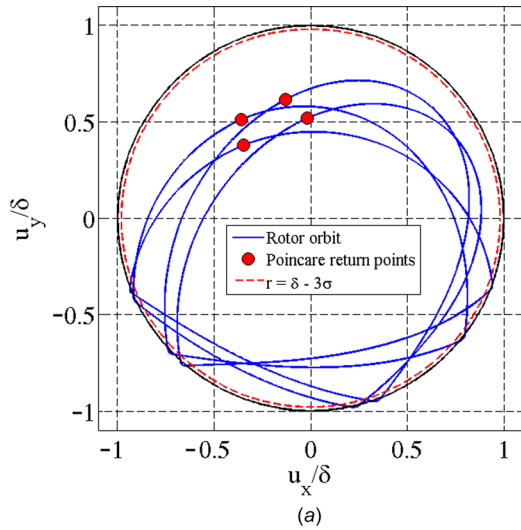
Fig. 6 Distinctions between rotor orbits using the LECM and JG models ($n = 1.7\omega_n$): (a) LECM ($k_c = 5 \times 10^8$ N/m), (b) JG rotor–stator rub model (full numeric simulation), and (c) JG rotor–stator rub model (exponential contact force fit)

The radial range of interest is then extracted by noting both the maximum radial deflection (i.e., minimum rotor–stator closeness) and the minimum radial deflection at which the contact force becomes non-negligible. Clearly, this approach requires heuristic

identification of the minimum bound of the radial deflection range of interest. Several trials may be necessitated before appropriate bounds are selected, as determined by comparing the rotor orbits found using full numeric simulation and the exponential curve fit.

For the case shown in Fig. 5, the minimum and maximum radial range over which to perform the regression are selected as $r = \delta - 4\sigma$ and $r = \delta - 2.5\sigma$, respectively. Using this radial range, the curve fit parameters defined in Eq. (12) are $a_0 = 0.0048$, $a_1 = 0.0075$, and $\lambda = 1.441$. The exponential fit is compared to the quasistatic contact force in Fig. 7, and displays excellent agreement. Still, the appropriate metric for assessing agreement between the two approaches extends beyond contact force agreement: the rotordynamics must likewise exhibit agreement. This comparison is provided in Figs. 6(b) and 6(c) for the full numeric simulation and exponential fit, respectively. As is evident from the figures, the rotor orbits are indeed both qualitatively and quantitatively similar, even for a chaotic response comprising numerous impacts.

4.2 Rotordynamic Differences Between the LECM to the JG Contact Models. Intuitively, similar responses are gleaned from the LECM and JG contact models when the number of contacts per revolution is small, as shown in Fig. 8 for a period-2 orbit at $n = 1.45\omega_n$, where ω_n is the natural frequency of the noncontacting Jeffcott rotor. The rotor deflection is normalized by the set-point clearance δ, which is represented on the orbit plots using a circle with a normalized radius of unity. Likewise, a reduced radius of $r = \delta - 3\sigma$ is shown with a dashed line to highlight the importance of properly accounting for surface roughness. Poincaré return points are obtained by sampling the nonautonomous system response once per normalized rotor rotation; i.e., a Poincaré return point is found every 2π nondimensional units of time.

As the number of contacts per revolution increases, the cumulative influence of different contact force models generates qualitatively different responses. For example, consider the rotor response using each contact model at $n = 1.7\omega_n$, shown in Fig. 6. The LECM predicts a period-4 response, while the JG rough surface rotor–stator rub model predicts chaotic motion, as evidenced by a scattering of the Poincaré return points and broadband frequency content (see Fig. 9).

Still, the qualitative differences between the models are best elucidated by observing displacements on the scale of the contact phenomena. A small portion of the full rotor orbits originally given in Fig. 6 is provided in Fig. 10, showing the rotor–stator impact on a much finer scale. In both figures, the set-point clearance δ is shown along with a chosen representation of surface roughness; i.e., a radial line at $r = \delta - 3\sigma$ (this is also shown with the LECM results to facilitate comparison, even though the
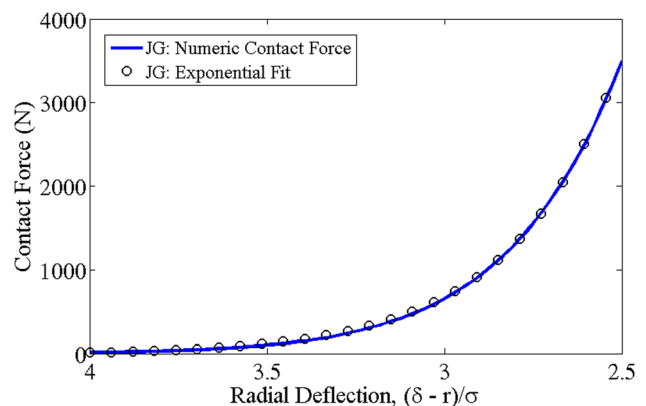

Fig. 7 Fitting an exponential function to the quasistatic contact force versus rotor radial deflection (expressed as the number of surface height standard deviations from the clearance; i.e., rotor–stator closeness)
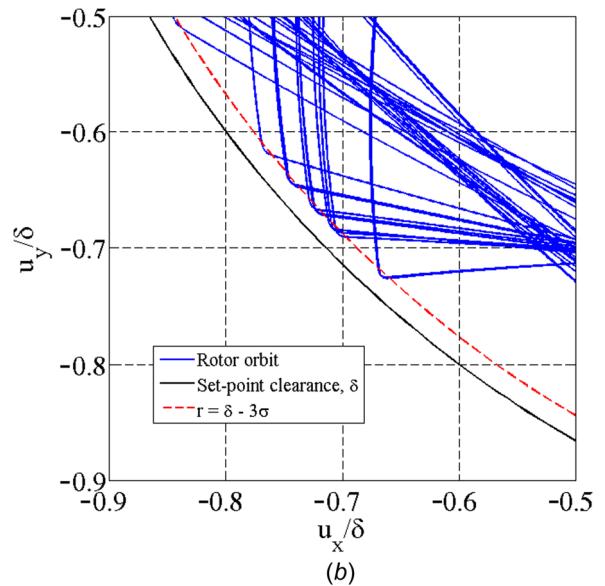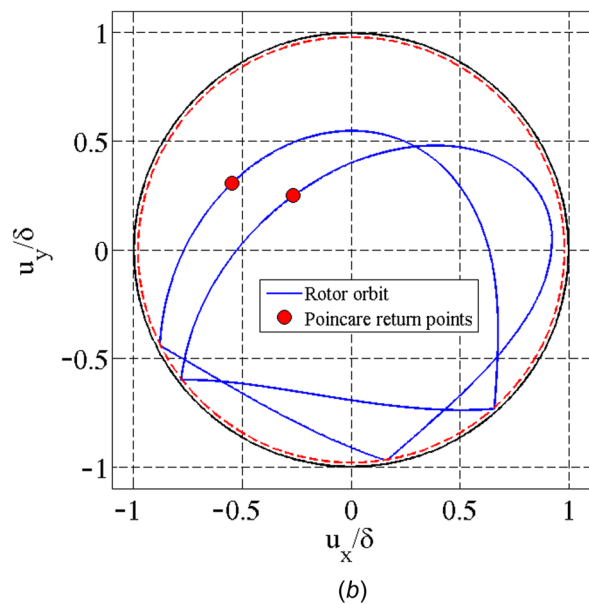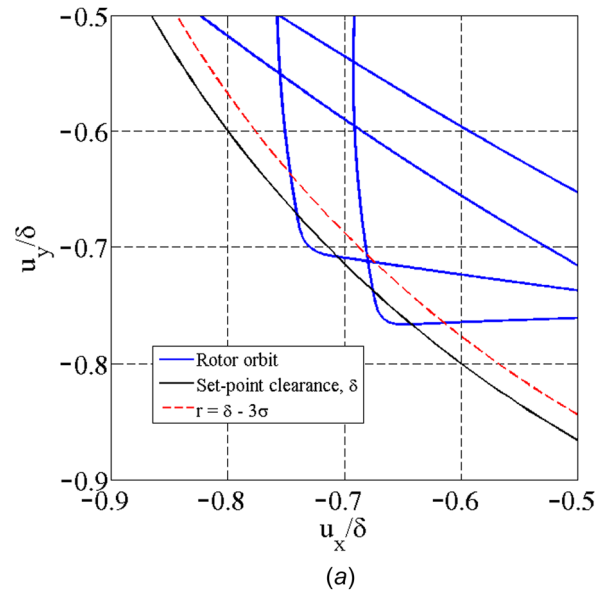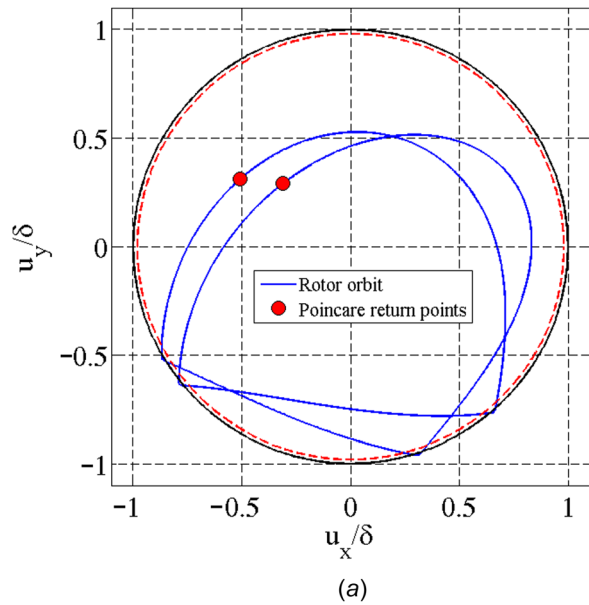
Fig. 8 Similarities between rotor orbits using the LECM and JG models ($n = 1.45\omega_n$): (a) LECM and (b) JG (exponential contact force fit)

Fig. 9 Broadband frequency spectra indicating the presence of chaotic response (JG model, $n = 1.7\omega_n$)

Fig. 10 Observing differences between the LECM and JG rotor–stator rub models on a finer scale ($n = 1.7\omega_n$): (a) LECM ($k_c = 5 \times 10^8$ N/m) and (b) JG rotor–stator rub model
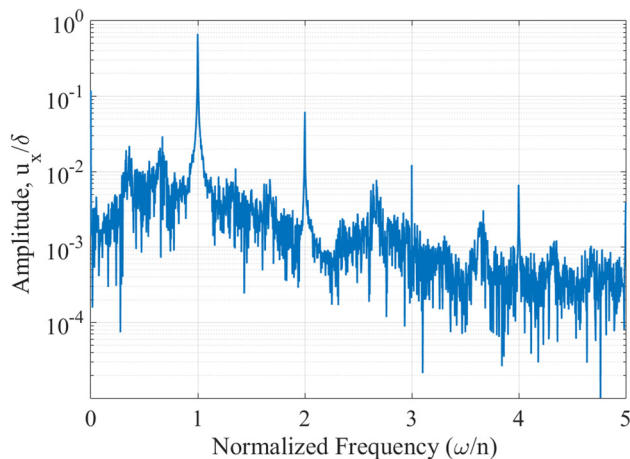
LECM does not account for surface roughness). The LECM rotor–stator contact force switches on immediately when the rotor deflection exceeds the set-point clearance, and henceforth the contact force depends only on the contact stiffness k_c and rotor–stator interference $r - \delta$. The JG rotor–stator rub model instead predicts a gradual increase in the contact force as the rotor–stator closeness approaches the surface roughness dimension. In fact, Fig. 10(b) shows that the rotor rebounds from the stator when only a small percentage of the asperities interact. This effective reduced clearance is likely critically important for rotor–stator systems with clearances near the surface roughness dimension.

Shaft speed bifurcation diagrams are a convenient tool for easily ascertaining broad differences between the LECM and JG rotor–stator rub models. The composite of all Poincaré return points over the considered parameter range provides the bifurcation diagram, which adeptly illuminates quantitative and qualitative changes in response with variations in the control parameter (in this case, shaft speed). The shaft speed bifurcation diagrams are given in Figs. 11(a) and 11(b) for the LECM and JG rotor–stator rub models, respectively. Though the figures display
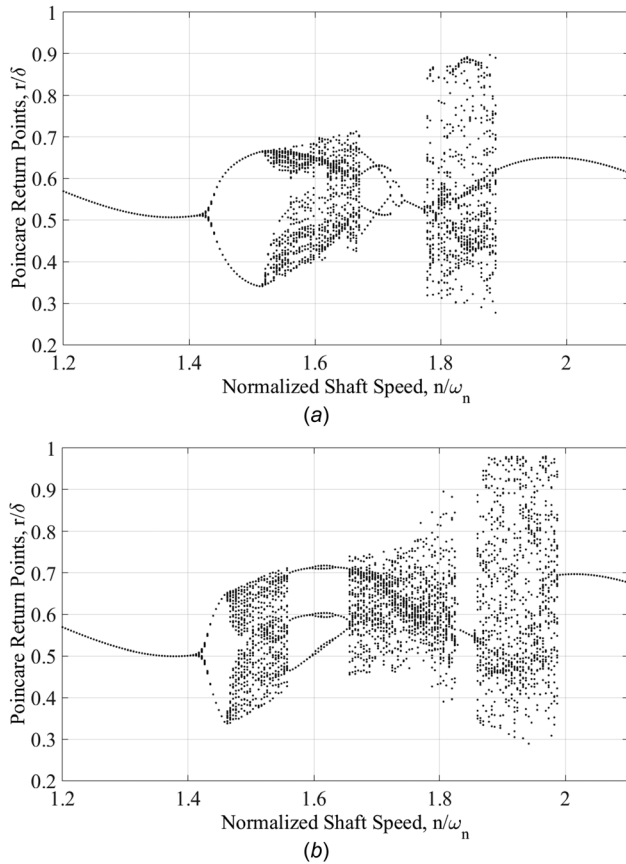
Fig. 11 Shaft speed bifurcation study (see Appendix B for surface and rotor parameters) (a) LECM ($k_c = 5 \times 10^8$ N/m) and (b) JG

some generic similarities, it is clear that the JG rotor–stator rub model predicts different responses than the LECM. Thus, when deciding on a contact model for a rotor–stator rub study, care must be taken in choosing whether the LECM is in fact appropriate. Each model begins by predicting a period-1 response until approximately $n = 1.42\omega_n$, at which point period-doubling is encountered, and the response bifurcates to period-2 motion. Beyond this point, the models begin to predict different responses. The JG model implementation shows, for the parameters considered here, a greater proclivity for chaotic motion (note the expanded shaft speed ranges over which chaos is observed). The differences could perhaps be attributed to the decreased likelihood of grazing bifurcations in the JG model, since the contact force varies smoothly (albeit over a small radial range) rather than being a truly piecewise-smooth dynamical system such as the LECM.

5 Conclusion

A prerequisite for accurately simulating rotor–stator rub is realistically modeling the contact phenomena. Two phenomena can dictate the contact physics: asperity deformation and/or bulk material deformation. Previous rotor–stator contact models such as the LECM indicate that bulk material deformation is the primary mechanism generating contact force. The LECM fails to satisfy the requirement of realistically modeling contact, relying instead on an esoteric contact stiffness in addition to assuming point contact. An alternative approach is presented which approximates the contact force using the JG elastoplastic rough surface contact model, founded upon measurable parameters of the rotor and stator surfaces. Interestingly, the results presented herein show that rotor rebound occurs when the rotor–stator separation distance is on the order of 3σ, implying that for partial rubs the primary mechanism of contact is actually asperity deformation. Thus, the

present model not only more realistically captures the contact force mathematically but also elucidates the primary contact physics dominating partial rotor–stator rubs: asperity deformation. Though some similarities exist between results found using the LECM and JG rotor–stator rub models, shaft speed bifurcations indicate significant deviations between the predicted rotor motions. Another advantage of modeling rotor–stator rub using a rough surface approach is the capability to isolate and investigate individual surface parameters. This capability could potentially be used to reduce the adverse influence of prolonged rub via enhanced surface engineering. Even though the newly develop JG rotor–stator rub model relies on measurable surface parameters to calculate the contact force, a necessary future step toward ascertaining a suitable rotor–stator rub model is experimental verification.

Nomenclature

B = rotor length
c = damping coefficient
E = composite elastic modulus
F_{cx}, F_{cy} = normal contact force
F_{fx}, F_{fy} = friction force
$h(\theta)$ = circumferential clearance
k = support stiffness
n = shaft speed
R = surface height standard deviation
R_r = rotor radius
u_x, u_y = rotor deflections in the x and y directions
δ = set-point clearance
ϵ = rotor eccentricity
η = areal density of asperities
θ = circumferential position
θ_m = angular location of minimum clearance
μ = friction coefficient
σ = surface height standard deviation
σ_s = asperity height standard deviation
ψ = plasticity index
ω_c = critical interference

Appendix A: Using the JG Model to Calculate the Rotor–Stator Contact Force

Real engineering surfaces are not smooth, but are instead a collection of peaks and valleys referred to as asperities. In the same manner as the historically venerable elastic GW model [29], the contact of two opposing rough surfaces is reduced to that of one rigid flat contacting a single rough surface whose parameters are a composite of both real rough surfaces. The asperity heights z are defined from the mean asperity height, and the separation distance between this mean and the contacting rigid flat at each rotor circumferential position θ is the circumferential clearance $h(\theta)$. The standard deviation of surface heights and asperity heights are σ and σ_s, respectively, and are related by

$$\sigma^2 = \sigma_s^2 + \frac{3.717 \times 10^{-4}}{\eta^2 R^2} \tag{A1}$$

where η is the composite areal asperity density and R is the composite average asperity radius of curvature [29]. The distance between the mean surface height and the mean asperity height is y_s (see Ref. [28]). Here, the asperity heights are presumed to obey a Gaussian distribution $\phi(z)$ without any loss of generality

$$\phi(z^*) = \frac{1}{\sqrt{2\pi}}\left(\frac{\sigma}{\sigma_s}\right)\exp\left[-0.5\left(\frac{\sigma}{\sigma_s}\right)^2(z^*)^2\right] \tag{A2}$$

where the superscript $(\cdot)^*$ signifies normalization by σ.

Jackson and Green [33] extended a finite element study of flattening elastoplastic hemispherical contact to a rough surface contact model, where hardness is shown to be a function of both geometry and material properties [30]. The interference between each asperity and the contacting rigid flat is $\omega = z - d$, where d is the general surface separation distance (here, $d = h(\theta)$). The critical interference ω_c at the initial point of yielding is derived from the von Mises yield criterion

$$\omega_c = \left(\frac{\pi C S_y}{2E}\right)^2 R \tag{A3}$$

The material Poisson's ratio is ν and the yield strength is S_y. Specifically, the product CS_y is chosen as $CS_y = \min(C(\nu_1)S_{y1}, C(\nu_2)S_{y2})$ [26], where, in this work surfaces, 1 and 2 represent the rotor and stator. The constant C is calculated to be

$$C = 1.295 \exp 0.736\nu \tag{A4}$$

Using the critical interference, the contact force at the point of initial yielding is

$$\bar{P}_c = \frac{4}{3}\left(\frac{R}{E}\right)^2 \left(\frac{1}{2}\pi C S_y\right)^3 \tag{A5}$$

where the over-bar signifies a single asperity model (i.e., contact between a sphere and a flat). Here, E is the composite elastic modulus for the contacting surfaces [29]. For small deformations, $0 \leq \omega/\omega_c \leq 1.9\omega_c$, the solution is essentially identical to the Hertzian model. For $\omega > 1.9\omega_c$, the contact force acting on a single asperity is

$$\bar{P} = \bar{P}_c \left\{ \left[\exp\left(-\frac{1}{4}\left(\frac{\omega}{\omega_c}\right)^{5/12}\right)\right]\left(\frac{\omega}{\omega_c}\right)^{3/2} + \frac{4H_G}{CS_y}\left[1 - \exp\left(-\frac{1}{25}\left(\frac{\omega}{\omega_c}\right)^{5/9}\right)\right]\left(\frac{\omega}{\omega_c}\right) \right\} \tag{A6}$$

where

$$\frac{H_G}{S_y} = 2.84\left[1 - \exp\left(-0.82\left(\sqrt{\frac{\omega}{R}}\left(\frac{\omega}{1.9\omega_c}\right)^{\frac{B}{2}}\right)^{-0.7}\right)\right] \tag{A7}$$

$$B = 0.14 \exp(23e_y) \tag{A8}$$

$$e_y = \frac{S_y}{E} \tag{A9}$$

Equation (A7) indicates that surface hardness H_G depends on both material and surface properties.

Still, Eq. (A6) only provides the contact force acting on a single asperity. When the rigid flat and composite rough surface are separated by a distance $d = h(\theta)$, any asperity whose height exceeds $h(\theta)$ contacts the rigid flat. Thus, the contribution of all asperities of height z toward the total contact force at circumferential location θ is

$$\tilde{P}(z, \theta) = \eta A_n \bar{P}(z - h(\theta))\phi(z) \tag{A10}$$

where A_n is the nominal contact area. Thus, the total contact force at a prescribed surface separation distance is found by summing the contribution of all asperities whose height exceeds the surface separation distance. Such a summation is achieved by integrating Eq. (A10) over the entire contact range

$$P(\theta) = \eta A_n \int_{h(\theta)}^{\infty} \bar{P}(z - h(\theta))\phi(z)\, dz \tag{A11}$$

Table 1   Rotordynamic parameters

Parameter	Value
Mass, m (kg)	1 kg
Damping ratio, ζ	0.4
Stiffness, k (N/m)	1×10^5 N/m
Eccentricity, ϵ (m)	0.8×10^{-4} m
Set-point clearance, δ (m)	1.6×10^{-4} m
Friction coefficient, μ	0.15
Rotor radius, R_r (m)	0.1 m
Rotor length, B (m)	0.1 m

Table 2   Surface parameters

Parameter	Value
Equivalent modulus, E (Pa)	25×10^9 Pa
Surface height stand. dev., σ (m)	1×10^{-6} m
Areal asperity density, η (asp./m^2)	5×10^{11} asp/m^2
Asperity radius, R (m)	2×10^{-6} m
Yield strength, S_y (Pa)	0.1×10^9 Pa

Since the surface separation distance $h(\theta)$ is a function of circumferential location, Eq. (A11) is evaluated separately at each circumferential location. Rather than evaluate the nominal contact area A_n for each discrete circumferential area considered, Eq. (A11) is redefined to calculate the average contact pressure, $\rho(\theta) = P(\theta)/A_n$

$$\rho(\theta) = \eta \int_{h(\theta)}^{\infty} \bar{P}(z - h(\theta))\phi(z)\, dz \tag{A12}$$

Now, Eq. (A12) is substituted into Eqs. (5) and (6) and integrated numerically to obtain the contact force acting on the rotor. It is imperative to note that the rub force considered herein is quasi-static, and neglects inertial effects at the asperities. The rub force therefore only depends on the rotor's position r; thus, a curve fit approximation of the rub force versus rotor deflection can impart a significant improvement in computational expediency.

Appendix B: Rotor and Stator Parameters

The rotor parameters used in this work are provide in Table 1, while the relevant surface roughness parameters are provided in Table 2. These parameters are calculated from real surface measurements [33].

References

[1] Green, I., and Casey, C., 2005, "Crack Detection in a Rotor Dynamic System by Vibration Monitoring: Part I—Analysis," ASME J. Eng. Gas Turbines Power, **127**(2), pp. 425–436.

[2] Varney, P., and Green, I., 2012, "Crack Detection in a Rotordynamic System by Vibration Monitoring—Part II: Extended Analysis and Experimental Results," ASME J. Eng. Gas Turbines Power, **134**(11), p. 112501.

[3] Varney, P., and Green, I., 2013, "Rotordynamic Crack Diagnosis: Distinguishing Crack Location and Depth," ASME J. Eng. Gas Turbines Power, **135**(11), p. 112101.

[4] Lee, A. S., and Green, I., 1994, "Higher Harmonic Oscillations in a Non-Contacting FMR Mechanical Face Seal Test Rig," ASME J. Vib. Acoust., **116**(2), pp. 161–167.

[5] Varney, P., and Green, I., 2014, "Rotor/Stator Rubbing Contact in an Overhung Rotordynamic System," STLE Annual Meeting, Lake Buena Vista, FL, May 18–22.

[6] Beatty, R. F., 1985, "Differentiating Rotor Response Due to Radial Rubbing," J. Vib., Acoust., Stress, Reliab. Des., **107**(2), pp. 151–160.

[7] Choy, F. K., and Padovan, J., 1987, "Nonlinear Transient Analysis of Rotor-Casing Rub Events," J. Sound Vib., **113**(3), pp. 529–545.

[8] Kim, Y. B., and Noah, S. T., 1990, "Bifurcation Analysis for a Modified Jeffcott Rotor With Bearing Clearances," Nonlinear Dyn., **1**(3), pp. 221–241.

[9] Chu, F., and Zhang, Z., 1997, "Bifurcation and Chaos in a Rub-Impact Jeffcott Rotor System," J. Sound Vib., **210**(1), pp. 1–18.

[10] Sawicki, J. T., Padovan, J., and Al-Khatib, R., 1999, "The Dynamics of Rotor With Rubbing," Int. J. Rotating Mach., **5**(4), pp. 295–304.

[11] Edwards, S., Lees, A. W., and Friswell, M. I., 1999, "The Influence of Torsion on Rotor/Stator Contact in Rotating Machinery," J. Sound Vib., **225**(4), pp. 767–778.

[12] Lin, F., Schoen, M. P., and Korde, U. A., 2001, "Numerical Investigation With Rub-Related Vibration in Rotating Machinery," J. Vib. Control, **7**(6), pp. 833–848.

[13] Karpenko, E. V., Wiercigroch, M., and Cartmell, M. P., 2002, "Regular and Chaotic Dynamics of a Discontinuously Nonlinear Rotor System," Chaos, Solitons, Fractals, **13**(6), pp. 1231–1242.

[14] Qin, W., Chen, G., and Meng, G., 2004, "Nonlinear Responses of a Rub-Impact Overhung Rotor," Chaos, Solitons, Fractals, **19**(5), pp. 1161–1172.

[15] Peng, Z. K., Chu, F. L., and Tse, P. W., 2005, "Detection of the Rubbing-Caused Impacts for Rotor-Stator Fault Diagnosis Using Reassigned Scalogram," Mech. Syst. Signal Process., **19**(2), pp. 391–409.

[16] Zhang, W. M., and Meng, G., 2006, "Stability, Bifurcation and Chaos of a High-Speed Rub-Impact Rotor System in MEMS," Sens. Actuators, **127**(1), pp. 163–178.

[17] Chang-Jian, C. W., and Chen, C. K., 2009, "Chaos of Rub-Impact Rotor Supported by Bearings With Nonlinear Suspension," Tribol. Int., **42**(3), pp. 426–439.

[18] Inayat-Hussain, J. I., 2010, "Bifurcations in the Response of a Jeffcott Rotor With Rotor-to-Stator Rub," ASME Paper No. ESDA2010-24453.

[19] Cao, J., Ma, C., Jiang, Z., and Liu, S., 2011, "Nonlinear Dynamic Analysis of Fractional Order Rub-Impact Rotor System," Commun. Nonlinear Sci. Numer. Simul., **16**(3), pp. 1443–1463.

[20] Abu-Mahfouz, I., and Banerjee, A., 2013, "On the Investigation of Nonlinear Dynamics of a Rotor With Rub-Impact Using Numerical Analysis and Evolutionary Algorithms," Procedia Comput. Sci., **20**, pp. 140–147.

[21] Chavez, J. P., and Wiercigroch, M., 2013, "Bifurcation Analysis of Periodic Orbits of a Non-Smooth Jeffcott Rotor Model," Commun. Nonlinear Sci. Numer. Simul., **18**(9), pp. 2571–2580.

[22] Groll, G. V., and Ewins, D. J., 2002, "A Mechanism of Low Subharmonic Response in Rotor/Stator Contact-Measurements and Simulation," ASME J. Vib. Acoust., **124**(3), pp. 350–358.

[23] Abu-Mahfouz, 1993, "Routes to Chaos in Rotor Dynamics," Ph.D. thesis, Case Western Reserve University, Cleveland, OH.

[24] Popprath, S., and Ecker, H., 2007, "Nonlinear Dynamics of a Rotor Contacting an Elastically Suspended Stator," J. Sound Vib., **308**, pp. 767–784.

[25] Varney, P., and Green, I., 2014, "Nonlinear Phenomena, Bifurcations, and Routes to Chaos in an Asymmetrically Supported Rotor-Stator Contact System," J. Sound Vib., **336**, pp. 207–226.

[26] Green, I., 2005, "Poisson Ratio Effects and Critical Values in Spherical and Cylindrical Hertzian Contact," Int. J. Appl. Mech. Eng., **10**(3), pp. 451–462.

[27] Varney, P., and Green, I., 2015, "Applying Rough Surface Contact of Curved Conformal Surfaces to Rotor-Stator Rub," 70th STLE Annual Meeting, Dallas, TX, May 17–21.

[28] Varney, P., and Green, I., 2015, "Rough Surface Contact of Curved Conformal Surfaces: An Application to Rotor-Stator Rub," ASME J. Tribol. (in press).

[29] Greenwood, J. A., and Williamson, J. B. P., 1966, "Contact of Nominally Flat Surfaces," Proc. R. Soc. A, **295**(1442), pp. 300–319.

[30] Jackson, R. L., and Green, I., 2005, "A Finite Element Study of Elasto-Plastic Hemispherical Contact," ASME J. Tribol., **127**(2), pp. 343–354.

[31] Chang, W. R., Etsion, I., and Bogy, D. B., 1987, "An Elastic-Plastic Model for the Contact of Rough Surfaces," ASME J. Tribol., **109**(2), pp. 257–263.

[32] Green, I., 2002, "A Transient Dynamic Analysis of Mechanical Seals Including Asperity Contact and Face Deformation," Tribol. Trans., **45**(3), pp. 284–293.

[33] Jackson, R. L., and Green, I., 2006, "A Statistical Model of Elasto-Plastic Asperity Contact Between Rough Surfaces," Tribol. Int., **39**(9), pp. 906–914.